# Unfolding the band structure of van der Waals heterostructures

Georgios Vailakis ®[*] and Georgios Kopidakis ®

*Department of Materials Science and Technology, University of Crete, GR-70013 Heraklion, Greece*
*and Institute of Electronic Structure and Laser, Foundation for Research and Technology–Hellas, GR-70013 Heraklion, Greece*

Layer-by-layer stacking of two-dimensional materials results in van der Waals heterostructures (vdWH) of nanometer thickness and clean interfaces that often exhibit exceptional properties and present novel challenges. We perform first-principles calculations using density functional theory to examine the electronic properties of vdWH consisting of graphene (Gr) and semiconducting transition metal dichalcogenide (TMD) monolayers at several twist angles. We describe in detail our methodology for the creation of simulation cells which are almost free of strain due to lattice mismatch (less than 1%) and for unfolding the electronic bands of the vdWH in a way that allows for a straightforward comparison with the electronic structure of the constituent monolayers. The weak interlayer interactions in $Gr/MoS_2$ and $Gr/WS_2$ heterobilayers leave the Gr and TMD band structures almost unaffected but move the Fermi level closer to the TMD conduction band minimum. Careful examination of transitions from direct to indirect band gaps for some twist angles reveals that these are due to very small strain remaining in the simulation cells. In $WS_2/MoS_2$ and $WSe_2/MoSe_2$ heterobilayers, interlayer interactions do not affect the conduction band minimum at K but lead to eigenenergy splitting and eigenstate hybridization at the valence band around the $\Gamma$ point, which is very sensitive to interlayer distance and determines whether the valence band maximum is at the $\Gamma$ or K point. Our results unveil a small redshift of the intralayer electronic transitions of TMDs when interacting with either Gr or other TMD monolayers.

## I. INTRODUCTION

Intense research activity on atomically thin two-dimensional (2D) materials reveals their fundamental importance and potential for technological breakthroughs. Following semi-metallic graphene (Gr) [1,2], semiconducting transition metal dichalcogenide (TMD) monolayers [3] have attracted great interest with their unique mechanical, electronic, and optoelectronic properties [4]. Stable TMD monolayers, obtained by exfoliation from layered materials and other fabrication methods, consist of covalently bonded $MX_2$ units ($M = $ Mo, W and $X = $ S, Se) arranged in honeycomb lattices. They exhibit direct electronic band gaps at the edge of the Brillouin zone (BZ), which become indirect in multilayers resulting in interesting dimensionality-dependent exciton physics [5,6]. Atomic thickness TMDs and their nanostructures are promising materials for devices such as transistors, photodetectors, sensors, light-emitting diodes, quantum computing elements, etc., with many prototypes already materialized [7–9] and the catalysis of important chemical reactions for clean energy and environment [10,11].

Thus, it is not surprising that among a large number of possible 2D materials [12], the main focus is on Gr and TMDs. Combining 2D materials in layered heterostructures gives rise to novel properties and phenomena [13,14], perhaps the most spectacular being superconductivity in magic-angle twisted graphene superlattices [15,16]. Vertically stacked monolayers interacting through van der Waals forces create an unlimited number of possibilities. Starting with Gr and hexagonal boron nitride, a wide-band-gap insulator, in order to obtain clean interfaces and contacts [17–19], a plethora of van der Waals heterostructures (vdWH) containing these materials and TMDs is under investigation [20–32]. Together with many opportunities, these vdWH present some serious challenges, both at a fundamental and a practical level, such as atomic and electronic structure modifications, strain, charge transfer, interlayer excitons, and moiré potentials.

In this article, we present a systematic theoretical investigation of Gr/TMD and TMD/TMD twisted heterobilayers based on first-principles calculations with density functional theory (DFT). More specifically, we examine the effective electronic band structure [31–38] of these vdWH and compare with the band structure of the individual monolayers constituting the heterobilayers. We carefully address issues such as lattice mismatch, strain, twist angle, and weak interlayer interactions, and we discuss experimental signatures of our theoretical findings. For this purpose, we construct computational supercells consisting of monolayer lattices with minimal strain, and we develop a method to unfold the band structure from the vdWH supercell BZ to the BZ of the monolayer primitive cells. Despite the fact that strong excitonic effects in TMDs require calculations beyond DFT with well-established theoretical methods, the electronic band structure is very well described by DFT, which gives electronic band gap values close to the optical gaps [4,39,40]. The inclu-
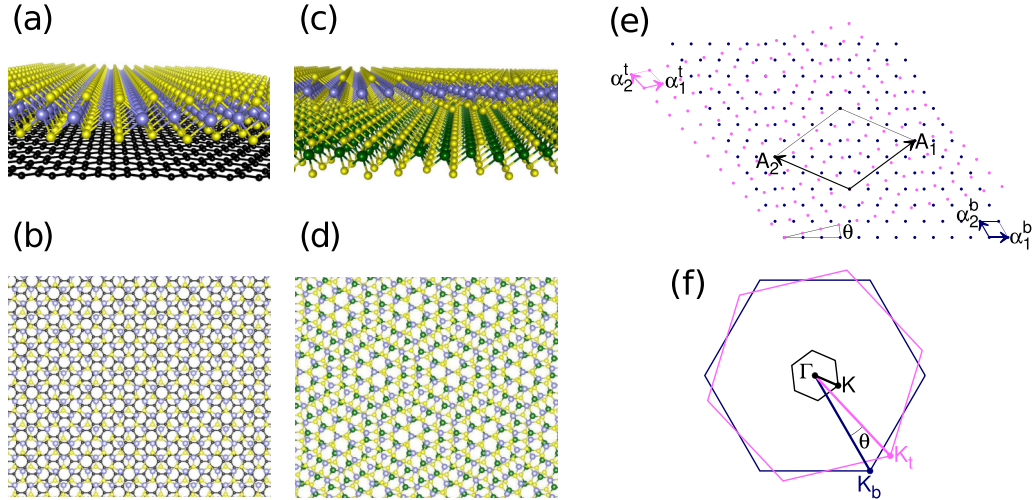
———————
[*]gvailakis@materials.uoc.gr

FIG. 1. Two examples of vdWH. (a) Gr/MoS$_2$@30 and (b) same, top view. (c) WS$_2$/MoS$_2$@13.18 and (d) same, top view. (e) Moiré pattern forming in WS$_2$/MoS$_2$@13.18 by combining the two hexagonal lattices with PC vectors $\boldsymbol{a}_1^b$, $\boldsymbol{a}_2^b$, $\boldsymbol{a}_1^t$, $\boldsymbol{a}_2^t$ (blue for bottom WS$_2$ and magenta for top MoS$_2$ monolayer). $\boldsymbol{A}_1$ and $\boldsymbol{A}_2$ are the lattice vectors of the SC, built from the transformation matrices $M_b = \left(\begin{smallmatrix} 5 & 3 \\ -3 & 2 \end{smallmatrix}\right)$ and $M_t = \left(\begin{smallmatrix} 5 & 2 \\ -2 & 3 \end{smallmatrix}\right)$ (see the text). (f) The PBZ of bottom (blue hexagon) and top (magenta hexagon) monolayers and the SBZ (black hexagon) of the SC for WS$_2$/MoS$_2$@13.18 with the K-Γ path for each BZ.

sion of spin-orbit coupling is straightforward but beyond the scope of this work. In Sec. II A we provide computational details for the implementation of DFT, in Sec. II B we describe the construction of our vdWH simulation cells, and in Sec. II C we present our method for electronic band structure unfolding. We present and discuss our results for Gr/$M$S$_2$ heterobilayers in Sec. III A, and for W$X_2$/Mo$X_2$ heterobilayers in Sec. III B. Finally, in Sec. IV we summarize our results.

## II. METHODS

### A. Density functional theory calculations

DFT calculations were performed within the projector augmented wave method (PAW) for core electrons and nuclei [41,42] and the generalized gradient approximation (GGA) of Perdew-Burke-Ernzerhof (PBE) for the exchange-correlation functional [43] using the Vienna Ab-initio Simulation Package (VASP) [44,45]. To take into account the van der Waals interactions between monolayers, the density-dependent correction dDsC [46,47] was used. Wave functions were expanded on a plane-wave basis set with a kinetic energy cutoff of 450 eV. Convergence criteria for the self-consistent calculations were set at $10^{-4}$ eV for the electronic part and $10^{-3}$ eV for the ionic relaxation. In the band structure calculations, the electronic convergence criterion was set at $10^{-7}$ eV. For the Brillouin zone sampling in a Gr monolayer, a $k$-point mesh of $25 \times 25 \times 1$ was used for the primitive cell (PC), which was appropriately scaled for every simulation cell (SC) with a different size so that the density of $k$-points remains similar. In all cases, periodic boundary conditions were applied with a vacuum of 20 Å added in the direction perpendicular to the monolayers to avoid interaction between periodic images.

### B. Simulation cells

We examine bilayer vdWH consisting of Gr and semiconducting TMD monolayers. More specifically, we present results for Gr stacked with $M$S$_2$ and for W$X_2$ with Mo$X_2$, where $M$ stands for molybdenum (Mo) or tungsten (W) and $X$ stands for sulfur (S) or selenium (Se). Atoms in these 2D materials are arranged in honeycomb lattices consisting of two hexagonal sublattices $A$ and $B$. In general, vertically stacked monolayers in the vdWH are not aligned and one lattice is rotated with respect to the other by a certain twist angle. We investigate the electronic properties of vdWH as a function of twist angle, $\theta$. Different lattice constants and twist angles create lattice mismatch between the two monolayers that induces strain, which is known to modify electronic properties [40,48,49], making it difficult to isolate the physically interesting effects of the weak interaction between the two monolayers. We construct SC in such a way as to minimize strain to less than 1%.

In Gr/$M$S$_2$ heterobilayers, lattice constants of the weakly interacting monolayers are very different, while in W$X_2$/Mo$X_2$ they are almost identical. Monolayer equilibrium lattice constants from our DFT calculations (see Table S1 in the Supplemental Material (SM) [50]) are in agreement with other works and close to experimental values [4,40]. Two examples of vdWH are shown in Fig. 1. We adopt the layered assemblies notation (LAN) [51] according to which the heterobilayer Gr/MoS$_2$ with a twist angle $\theta = 30°$ of Figs. 1(a) and 1(b) is denoted by Gr/MoS$_2$@30, and the heterobilayer WS$_2$/MoS$_2$ with $\theta = 13.18°$ of Figs. 1(c) and 1(d) is denoted by WS$_2$/MoS$_2$@13.18. To construct our SC, two monolayers with primitive lattice vectors $\boldsymbol{a}_1^b$, $\boldsymbol{a}_2^b$ and $\boldsymbol{a}_1^t$, $\boldsymbol{a}_2^t$, with $b$ and $t$ corresponding to bottom and top, respectively, are stacked with the top monolayer rotated by a twist angle
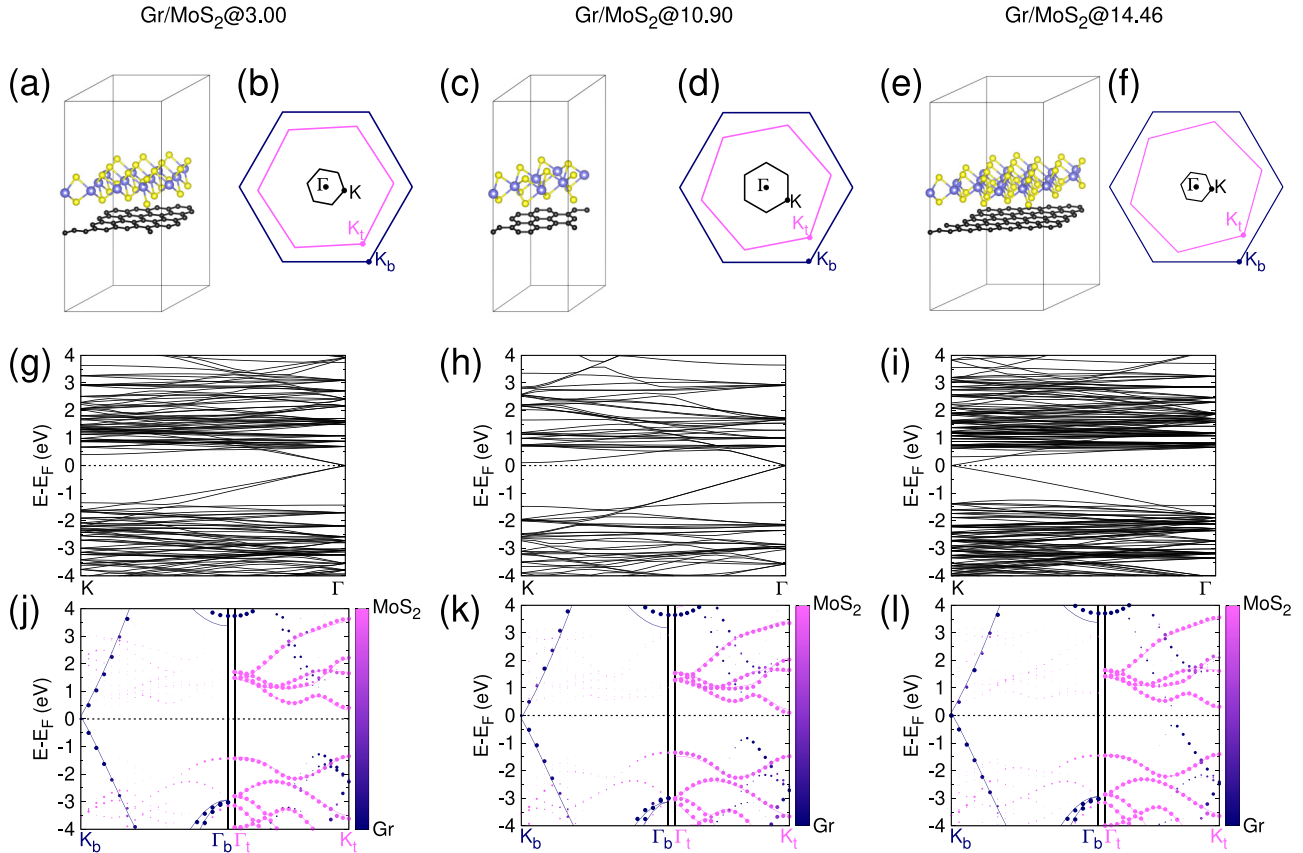
FIG. 2. The SC of Gr/MoS$_2$ at three different twist angles 3.00° (a), 10.90° (c), and 14.46° (e), and their corresponding SBZ (black), PBZ of Gr (blue), and MoS$_2$ (magenta) in (b), (d), and (f). The standard band structure at the SBZ for twist angles 3.00° (g), 10.90° (h), and 14.46° (i) and the corresponding effective band structure (EBS) projected on the two PBZ (j), (k), and (l).

$\theta$, as shown in Fig. 1(e). A choice for the monolayer PC consists of an atom of the hexagonal sublattice $A$ (transition metal atom for TMDs) at zero and an atom of the hexagonal sublattice $B$ (chalcogen atom for TMDs) at $\frac{2}{3}\boldsymbol{a_1} + \frac{1}{3}\boldsymbol{a_2}$ (indices for bottom and top sometimes omitted for the sake of notational simplicity). To minimize lattice mismatch in the vdWH, we search for SC lattice vectors in both monolayers [top and bottom, blue and magenta points, respectively, in Fig. 1(e)] that are almost equal, i.e., $\boldsymbol{R_b} \approx \boldsymbol{R_t}$, where $\boldsymbol{R_b} = n_1^b\boldsymbol{a_1^b} + n_2^b\boldsymbol{a_2^b}$ and $\boldsymbol{R_t} = n_1^t\boldsymbol{a_1^t} + n_2^t\boldsymbol{a_2^t}$ ($n_i^b$, $n_i^t$ are integers). We define the SC vector $A$ as a sum of two vectors of equal magnitude, $\boldsymbol{A_1} \equiv \frac{\boldsymbol{R_b}+\boldsymbol{R_t}}{2}$ and $\boldsymbol{A_2}$, at an angle of 120° with respect to $\boldsymbol{A_1}$ with $|\boldsymbol{A_1}| = |\boldsymbol{A_2}| = A$ thus preserving hexagonal lattice symmetry as shown in Fig. 1(e). The lattice mismatch is defined as $\delta_{\text{tot}} = \frac{|\boldsymbol{R_b}|-|\boldsymbol{R_t}|}{A}$ so that the small remaining strain is equally distributed as isotropic for the two monolayers, i.e., $\delta_b = \frac{|A|-|\boldsymbol{R_b}|}{A}$ for the bottom and $\delta_t = \frac{|A|-|\boldsymbol{R_t}|}{A} = -\delta_b$ for the top monolayer. In vdWH, under certain conditions, atoms in each monolayer are displaced from their ideal honeycomb lattice positions [52]. The stacking of monolayers and the atomic positions depend on the twist angle [53]. For instance, at twist angles smaller than 6° for homo-bilayers (same monolayers stacked up), there is a coupling of the phonons between the monolayers [54], which changes atomic positions. Our study concerns vdWHs at twist angles where the monolayers can be thought of as rigid Lego blocks [13]. Therefore, in our

SC, atomic coordinates in the periodic directions are fixed at the monolayer values, and only the vertical positions of the atoms are allowed to relax, along the axis perpendicular to the monolayers.

### C. Band unfolding

The main challenge in studying the electronic properties of vdWH is interpreting band structure diagrams. The first Brillouin zone (BZ) of the SC (SBZ) is different from the BZ of the PC (PBZ), as shown in Fig. 1(f). Standard DFT electronic structure calculations provide electronic bands that are folded in the SBZ. Examples of such "spaghetti" diagrams are presented in Figs. 2(g)–2(i), where the bands fold into the smaller SBZ, and the resulting band structures are difficult to interpret. For instance, in Figs. 2(g) and 2(h), the Dirac cone of Gr is not located at the K point of the SBZ. Thus, the folded bands of vdWH make a comparison with band structures of the isolated monolayers troublesome. While the band structure calculation is performed in the SBZ, we want to perform the sampling and present the bands in the PBZ. The solution is to calculate the effective band structure (EBS) [31–38] that unfolds the bands by projecting the electronic states from the SBZ to the PBZ. Within this approach, outlined in what follows, we can compare with one-to-one correspondence the EBS of vdWH with the band structures of isolated monolayers, as shown in

Figs. 2(j)–2(l). We define the transformation matrices $M_b$, $M_t$ from monolayer PC vectors to SC lattice vectors,

$$\begin{bmatrix} A_1 \\ A_2 \end{bmatrix} = M_b \begin{bmatrix} a_1'^b \\ a_2'^b \end{bmatrix} = M_t \begin{bmatrix} a_1'^t \\ a_2'^t \end{bmatrix}, \qquad (1)$$

where $a_{1,2}'^{b,t} = (1 + \delta_{b,t}) a_{1,2}^{b,t}$ are the PC and $A_{1,2}$ are the SC reciprocal lattice vectors. In the reciprocal space, the corresponding BZ vectors are related through the transformation matrices

$$\begin{bmatrix} B_1 \\ B_2 \end{bmatrix} = (M_b^{-1})^T \begin{bmatrix} b_1'^b \\ b_2'^b \end{bmatrix} = (M_t^{-1})^T \begin{bmatrix} b_1'^t \\ b_2'^t \end{bmatrix}. \qquad (2)$$

The determinant of the transformation matrix gives the ratio between the volumes of the two unit cells $|M| = V_{SC}/V_{PC}$ and also suggests the degree of folding of the PBZ inside the SBZ. The number of PBZ $k_i$ points that fold at the same point $K$ inside the SBZ are $N_{fold} = |M|$, with $k_i = K + G_i$, where $i = 1, 2, \ldots, N_{fold}$ and $G = n_1 B_1 + n_2 B_2$. Each eigenvalue $E_{K,\nu}$ has infinite values of wave vector $q = K + G$ with different weight in a plane-wave expansion. This can be thought of as an unfolding to the infinite reciprocal space. The translational symmetry of the PBZ suggests which weights contribute to refolding from the infinite reciprocal space to the PBZ,

$$P_{K,\nu}(k) = \sum_g |C_{K,\nu}(g + k)|^2, \qquad (3)$$

where $C_{K,\nu}$ is the coefficient in the plane-wave expansion of the electronic state $K$, $\nu$, and $g = n_1 b_1' + n_2 b_2'$ are all the linear combinations of the PC reciprocal lattice vectors. $P_{K,\nu}(k)$ in Eq. (3) is the projection of the SC eigenstates (expanded in a plane-wave basis set) on the PC eigenstates, and it expresses the amount of the $K$, $\nu$ state that unfolds to $k$.

If $P$ is nonzero, then the state unfolds from point $K$ to $k$. The EBS is calculated from the spectral function

$$A(k, E) = \sum_\nu P_{K,\nu}(k) \delta(E_{K,\nu} - E). \qquad (4)$$

The selection of $K$-points in the SBZ is done in such a way that they unfold on the $k$-points we have selected, or $K_i = k_i - G$, where $G$ are all the linear combinations of the reciprocal lattice vectors for the SBZ, and $k_i$ ($K_i$) are points inside the PBZ (SBZ).

The difference between the band structure diagrams along paths in the SBZ, as obtained from DFT, and the EBS diagrams along high symmetry paths in the PBZs of the individual monolayers, as produced by our unfolding procedure, is illustrated in Fig. 2 for three SCs of Gr/MoS$_2$ at different twist angles. SC atomic configurations are shown in Figs. 2(a), 2(c) and 2(e), and corresponding SBZs and PBZs are shown in Figs. 2(b), 2(d) and 2(f). The spaghetti diagrams (folded bands) of Figs. 2(g)–2(i) along the K-Γ path of the SBZs, which are impossible to interpret, become clear EBS diagrams shown in Figs. 2(j)–2(l) along the K-Γ paths of the PBZs. Isolated monolayer band structures are also shown (solid lines). In our EBS plots, the projection of electronic states on each monolayer, i.e., their spectral weight, is indicated by the size of the circular points, according to Eq. (3). Color indicates the spatial location of the state with

TABLE I. The structures Gr/$MS_2$, with $M$ = Mo, W in the LAN notation, and the transformation matrices that create the SC from the primitive lattice vectors.

| | | | | Structures Gr/$MS_2$, $M$ = Mo, W | | | | |
| LAN | $m_{11}^b$ | $m_{12}^b$ | $m_{21}^b$ | $m_{22}^b$ | $m_{11}^t$ | $m_{12}^t$ | $m_{21}^t$ | $m_{22}^t$ |
|---|---|---|---|---|---|---|---|---|
| Gr/$MS_2$@3.00 | 5 | 4 | −4 | 1 | 4 | 3 | −3 | 1 |
| Gr/$MS_2$@10.90 | 4 | 2 | −2 | 2 | 3 | 1 | −1 | 2 |
| Gr/$MS_2$@14.46 | 6 | 5 | −5 | 1 | 5 | 3 | −3 | 2 |
| Gr/$MS_2$@24.80 | 5 | 1 | −1 | 4 | 3 | −1 | 1 | 4 |
| Gr/$MS_2$@27.64 | 6 | 5 | −5 | 1 | 5 | 2 | −2 | 3 |
| Gr/$MS_2$@30.00 | 6 | 3 | −3 | 3 | 4 | 0 | 0 | 4 |
| Gr/$MS_2$@32.36 | 6 | 1 | −1 | 5 | 3 | −2 | 2 | 5 |
| Gr/$MS_2$@35.20 | 5 | 4 | −4 | 1 | 4 | 1 | −1 | 3 |
| Gr/$MS_2$@45.54 | 6 | 1 | −1 | 5 | 2 | −3 | 3 | 5 |
| Gr/$MS_2$@49.10 | 4 | 2 | −2 | 2 | 2 | −1 | 1 | 3 |
| Gr/$MS_2$@57.00 | 5 | 1 | −1 | 4 | 1 | −3 | 3 | 4 |

respect to the monolayers. The color of each point represents its position in the direction perpendicular to the monolayers, i.e., it is the expectation value of this real space coordinate. In our color code, blue is for the bottom and magenta is for the top monolayer, with intermediate colors for positions in between. The characteristic features of our EBS representation are illustrated in Figs. 2(j)–2(l). It is clear that, since Gr and MoS$_2$ have different periodicities, when plotting along a high symmetry path in the PBZ of one layer, the weights of states corresponding to the other layer are smaller in general. There are, however, states from one layer unfolding in the path of PBZ of the other layer. When periodicities and orientations are very similar, it is possible that the weight of states (size of points) will be very similar along both PBZ paths. In fact, in vdWH consisting of monolayers with the same periodicity and orientation, this weight is the same along both PBZ paths (see the SM [50], Figs. S3 and S4 for W$X_2$/Mo$X_2$@0.00 and W$X_2$/Mo$X_2$@60.00, where PBZs are aligned).

EBSs for vdWH in a path of the PBZ of monolayers have been presented in previous works [31,32]. In this work, EBS representation is different: EBSs are plotted separately in the PBZ of each monolayer, and the size and color of points indicate their weight and position with respect to monolayers, respectively. We believe that this representation gives a clear picture of the electronic structure resulting from interaction between monolayers and helps identify possible interlayer and intralayer electronic transitions.

The SCs we examine here are presented in Table I for Gr/$MS_2$ and Table II for W$X_2$/Mo$X_2$, where we show the transformation matrices ($M_b$ and $M_t$) for the formation of each vdWH. The number of atoms of each case can be found in Table S2 of the SM [50].

## III. RESULTS

### A. Gr/$MS_2$ heterobilayers

After resolving issues associated with lattice mismatch between Gr and TMD monolayers as explained in the previous section, our SC bilayers are almost commensurate and unstrained. In agreement with previous studies, our results

TABLE II. The structures $WX_2/MoX_2$ with $X$ = S, Se in the LAN notation and the transformation matrices that create the SC from the primitive lattice vectors.

| | | | | Structures $WX_2/MoX_2$, $X$ = S, Se | | | | |
|---|---|---|---|---|---|---|---|---|
| LAN | $m_{11}^b$ | $m_{12}^b$ | $m_{21}^b$ | $m_{22}^b$ | $m_{11}^t$ | $m_{12}^t$ | $m_{21}^t$ | $m_{22}^t$ |
| $WX_2/MoX_2$@0.00 | 1 | 0 | 0 | 1 | 1 | 0 | 0 | 1 |
| $WX_2/MoX_2$@13.18 | 5 | 3 | −3 | 2 | 5 | 2 | −2 | 3 |
| $WX_2/MoX_2$@17.90 | 6 | 1 | −1 | 5 | 5 | −1 | 1 | 6 |
| $WX_2/MoX_2$@21.78 | 3 | 2 | −2 | 1 | 3 | 1 | −1 | 2 |
| $WX_2/MoX_2$@27.80 | 4 | 1 | −1 | 3 | 3 | −1 | 1 | 4 |
| $WX_2/MoX_2$@32.20 | 4 | 3 | −3 | 1 | 4 | 1 | −1 | 3 |
| $WX_2/MoX_2$@38.22 | 3 | 1 | −1 | 2 | 2 | −1 | 1 | 3 |
| $WX_2/MoX_2$@42.10 | 6 | 5 | −5 | 1 | 6 | 1 | −1 | 5 |
| $WX_2/MoX_2$@46.82 | 5 | 2 | −2 | 3 | 3 | −2 | 2 | 5 |
| $WX_2/MoX_2$@60.00 | 1 | 0 | 0 | 1 | 0 | −1 | 1 | 1 |

confirm that the interaction between Gr and TMD states is weak. This is clearly visible in the EBS we obtain. In addition to Fig. 2, with Gr/MoS$_2$ SCs shown together with the corresponding Brillouin zones and band structures, Fig. 3 presents another two representative EBSs (the rest can be found in the SM, Figs. S1 and S2 [50]). The EBS for Gr/MoS$_2$@30.0 of Fig. 3(a) clearly shows that the Dirac point of Gr almost coincides in energy with the conduction band minimum (CBM) of MoS$_2$. For different twist angles the CBM is slightly higher, but this proximity is a common feature in our Gr/MoS$_2$ vdWH. For Gr/WS$_2$, such as in Fig. 3(b), this feature is there but less pronounced, i.e., the CBM is more than 0.5 eV higher than the Fermi level of the vdWH.

We find significant variations in the TMD electronic bandgap energy, $E_g$, at different twist angles, $\theta$. Even though strain is negligible in our vdWHs, we further examine its effect since it is well known that it strongly affects monolayer TMD electronic properties [40]. Our calculations give a weak attraction between monolayers with small interface energies (of the order of a few tens of meV/Å$^2$; see Table S3 in the SM [50]) and small variation of equilibrium distance between Gr and TMD as a function of the twist angle, with values in good agreement with previous theoretical [30] and experimental [27,28] results. After SC relaxation in the direction perpendicular to the monolayers, C-atoms of Gr and $M$-atoms of the
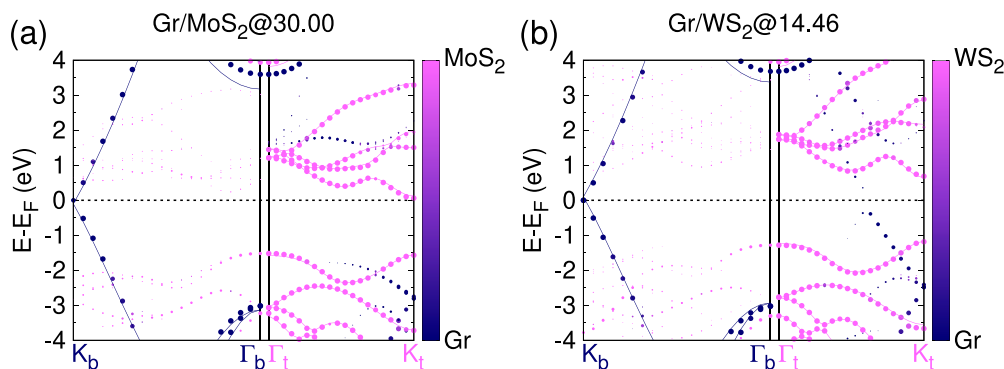


FIG. 4. Interlayer distance ($d$) for Gr/MoS$_2$ (a) and Gr/WS$_2$ (b), strain ($\delta_t$) (c), electronic energy band gaps ($E_g$) for Gr/MoS$_2$ (d), and for Gr/WS$_2$ (e), conduction band minimum (CBM) of the TMD monolayers (e) in the Gr/$MS_2$ bilayers as a function of the twist angle ($\theta$). In (d), (e), and (f), black and gray horizontal lines refer to MoS$_2$ and WS$_2$ monolayers, respectively.

TMD monolayer are on practically well-defined planes (standard deviation of the order of 0.01 Å). The variation of the interlayer distance, $d$, defined as the distance of the $M$-atom plane from Gr as a function of $\theta$ is presented in Fig. 4(a) for



FIG. 3. EBS of Gr/MoS$_2$@30.00 (a) and Gr/WS$_2$@14.46 (b). EBS of heterostructure with points, monolayer band structure with continuous lines, color code bars indicate real spatial location in the direction perpendicular to monolayers.
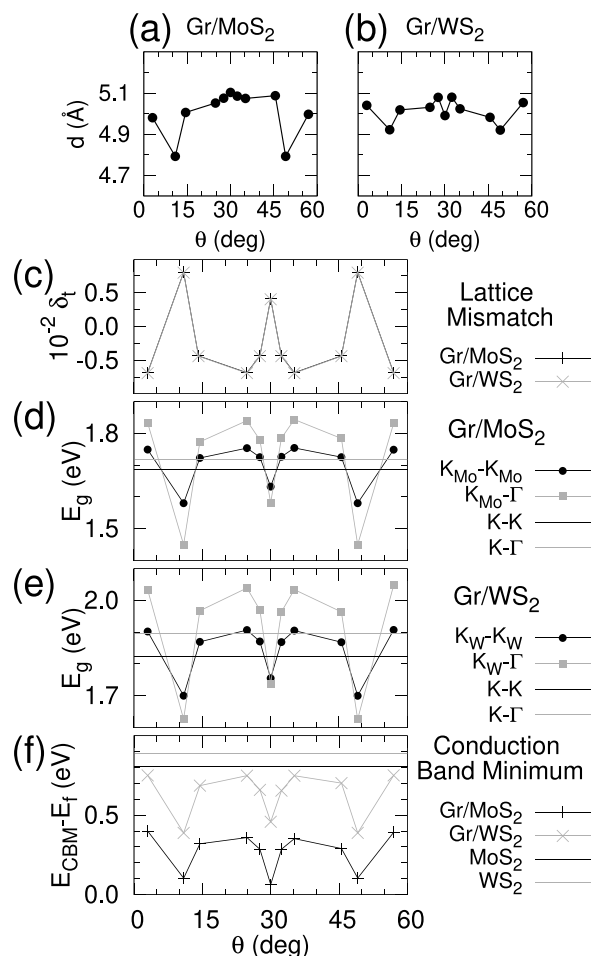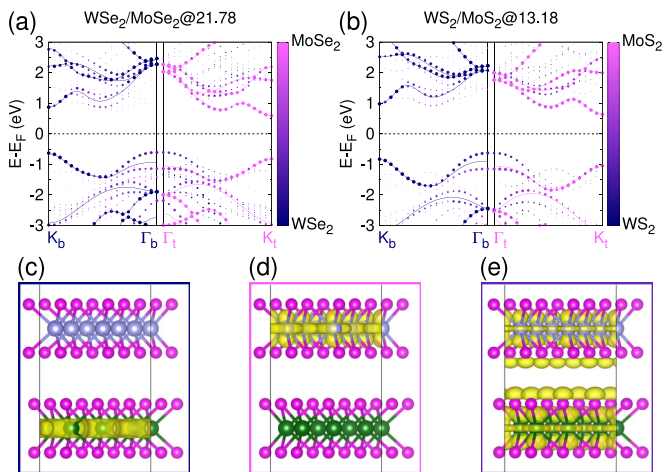
FIG. 5. EBS of WSe$_2$/MoSe$_2$@21.78 (a) and WS$_2$/MoS$_2$@13.18 (b), EBS of heterostructure with points, monolayer band structure with continuous lines, color code bars indicate real spatial location in the direction perpendicular to monolayers. Real space eigenstates corresponding to points in the EBS of (a). Highest occupied state at K$_b$ (WSe$_2$, blue point) in (c), lowest unoccupied state at K$_t$ (MoSe$_2$, magenta point) in (d), and highest occupied state at $\Gamma_b$ (purple point) in (e).

Gr/MoS$_2$ and in Fig. 4(b) for Gr/WS$_2$. Differences in values of $d$ are of the order of 0.1 Å and somewhat larger for certain twist angles and for Gr/MoS$_2$.

As shown in Fig. 4(c), strain remains much smaller than 1% for all twist angles. Electronic states of Gr close to the Dirac point do not change in the vdWH. However, for the TMDs, band gap changes are of the order of hundreds of meV, as shown in Fig. 4(d) for Gr/MoS$_2$ and in Fig. 4(e) for Gr/WS$_2$. These changes are correlated with the variation of strain in the SCs shown in Fig. 4(c) The band gap is redshifted for positive $\delta_t$ and blueshifted for negative $\delta_t$ in agreement with previous theoretical work [40]. Although strain is minimal in our SC, the resulting band gap variation is quite significant and is mainly due to the lowering of the CBM presented in Fig. 4(f). For some angles there is even a transition from direct to indirect band gap, i.e., from both the CBM and the valence band maximum (VBM) being at K to the CBM remaining at K and the VBM moving to $\Gamma$. If we assume that for small strain (i.e., ∼1%) the shift of the TMDs energy gap is linear [40], a linear fit of all vdWH (see Figs. S5 and S6 of the SM [50]) indicates a ∼10 meV redshift for both $M$S$_2$, similar to experiments [26]. According to our results, what emerges as universal behavior in Gr/$M$S$_2$ bilayers is that the Fermi level is close to the $M$S$_2$ CBM.

### B. W$X_2$/Mo$X_2$ heterobilayers

We present results for bilayers consisting of TMD monolayers with different metal but the same chalcogen atoms, i.e., W$X_2$/Mo$X_2$, where $X =$ S, Se. Since monolayer lattice constants are almost the same, these vdWH are almost free of strain. Representative EBS for W$X_2$/Mo$X_2$ are presented in Fig. 5(a) for WSe$_2$/MoSe$_2$@21.78 and in Fig. 5(b) for WS$_2$/MoS$_2$@13.18 (EBS for all of our SCs are presented in Figs. S3 and S4 of the SM [50]). Corresponding mono-
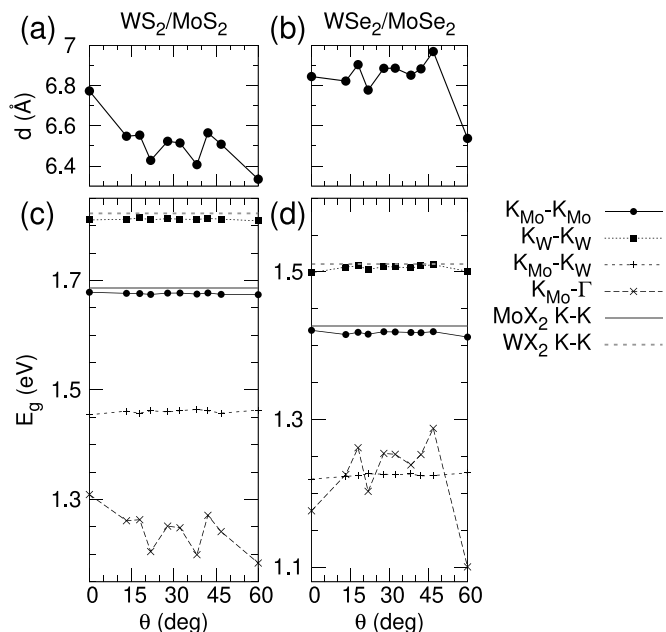


FIG. 6. Interlayer distance ($d$) for WS$_2$/MoS$_2$ in (a) and WSe$_2$/MoSe$_2$ in (b), electronic state energy differences ($E_g$) for WS$_2$/MoS$_2$ in (c) and WSe$_2$/MoSe$_2$ in (d) for W$X_2$/Mo$X_2$ bilayers as a function of the twist angle ($\theta$). Points connected with lines indicate results from the EBS of the vdWH, horizontal lines from monolayer band structure.

layer band structures are plotted with straight lines. Our results are in overall agreement with previous findings, which point to a type-II alignment interpretation for the bands of W$X_2$/Mo$X_2$, i.e., VBM and CBM at the edge of the PBZ zone are in different layers of the vdWH. This is shown in the examples of Fig. 5, where CBM is at K$_t$ of Mo$X_2$ while VBM is at K$_b$ of WSe$_2$ for WSe$_2$/MoSe$_2$@21.78 in Fig. 5(a), and at $\Gamma_b$ of WS$_2$ of WS$_2$/MoS$_2$@13.18 in Fig. 5(b).

Our EBS diagrams contain information about the projection of each $k$-point on each PBZ, obtained from Eq. (3), in the size of the plot point and about the position in its color. Examples of three real space eigenstates corresponding to points of Fig. 5(a) are presented. In Fig. 5(c), the highest occupied state at K$_b$ (blue point) is spatially located at the bottom monolayer, WSe$_2$. In Fig. 5(d), another extreme case is presented where the lowest unoccupied state at K$_t$ (magenta point) is spatially located at the top monolayer, MoSe$_2$. An eigenstate spread in both monolayers, i.e., the highest occupied state at $\Gamma_b$ (purple point), is presented in Fig. 5(e). The electronic structure as a function of the twist angle exhibits a rich behavior. Unlike Gr/TMD, lattice mismatch is practically zero (0.009% for $X =$ S and 0.07% for $X =$ Se) here and so is strain. However, EBS changes with $\theta$ due to changes in interlayer distance. After relaxing atomic positions in the direction perpendicular to the monolayers of our vdWH SCs, metal atoms remain on well-defined planes, and the interlayer distance $d$ is measured from W to Mo planes. In Figs. 6(a) and 6(b), the interlayer distance for WS$_2$/MoS$_2$ and WSe$_2$/MoSe$_2$, respectively, is plotted as a function of the twist angle. The values of $d$ are in overall agreement with experimental results [20,29],

and variation with $\theta$ is small. In the cases of 0° and 60°, deviations in the values of $d$ are more significant due to the very different stacking of "aligned" monolayers. In our SCs, for twist angle $\theta = 0°$ the transition metal is always on top of a transition metal and the chalcogen is on top of a chalcogen (*AA* stacking), while for $\theta = 60°$ the *M*-atom is again on top of the *M*-atom but *X* is at the center of the hexagon in the *xy*-plane formed from the atoms of the other monolayer ($B^{M/M}$ stacking).

Some important features of the dependence of electronic structure on twist angle are summarized in Figs. 6(c) and 6(d) for $WS_2/MoS_2$ and $WSe_2/MoSe_2$, respectively, where differences between conduction and valence band energies, $E_g$, at the high symmetry points $\Gamma$ and K of the PBZs (direct and indirect band gaps) are plotted as a function of $\theta$ (points connected with lines, which are a guide to the eye). We did not find CBM and/or VBM at any other *k*-points along the $\Gamma$-K path. The relevant energy differences for monolayers are shown with horizontal lines for comparison. In both cases, this energy difference at the edge of the PBZ does not change significantly with respect to the monolayer values. In Fig. 6(c), the direct band gaps at K of the $MoS_2$ (gray solid horizontal line at $E_g = 1.685$ eV) and at K of the $WS_2$ (gray dashed horizontal line at $E_g = 1.822$ eV) monolayers are reduced by $\sim$10 meV for the intralayer transitions in the vdWH, as shown by circles and squares connected with black solid and gray dashed lines, respectively. Similarly, in Fig. 6(d), the intralayer transitions for $MoSe_2$ (gray solid horizontal line at $E_g = 1.427$ eV) and $WSe_2$ (gray dashed horizontal line at $E_g = 1.511$ eV) are also redshifted in vdWH by about $\sim$10 meV. The TMD intralayer electronic transitions change slightly with the introduction of the other monolayer by redshifting of the order of 10 meV, as observed experimentally [22].

Lattice matching in $WX_2/MoX_2$ allows for the effects of the interaction between monolayers to become dominant, as opposed to strain effects in $Gr/MS_2$. This interaction splits energy eigenvalues around the $\Gamma_b$ and $\Gamma_t$ points of Fig. 5(a) and the eigenstates spread in both monolayers as seen in Fig. 5(e). Similarly, such a split is also present in the conduction band at the $K_b$-$\Gamma_b$ path of the $WX_2$ PBZ. These energy splits are the reason why $MX_2$ become direct gap semiconductors in their monolayer form. In [6], it is argued that the transition of direct to indirect band gap semiconductor of single to multilayer $MoS_2$ is caused by the combination of Mo-*d* and S-$p_z$ orbitals near the $\Gamma$ point. The split was discussed in [31], where it was examined how it changes with the interlayer distance. This is the reason why the band gap changes at different twist angles. In Figs. 6(c) and 6(d), the smallest energy transition

for all $WS_2/MoS_2$ is $K_t$-$\Gamma$ and for $WSe_2/MoSe_2$ it is $K_t$-$K_b$ (interlayer transition) for most twist angles, suggesting that interlayer transitions are more likely in $WSe_2/MoSe_2$ than $WS_2/MoS_2$. In both cases of $WX_2/MoX_2$, the interlayer transitions $K_b$-$K_t$ display a small variation ($\sim$6 meV) as a function of the twist angle. We find this interlayer transition at 1.46 eV for $X = S$ with experimental values at 1.4–1.5 eV [20,23] and 1.22 eV for $X = Se$ with experimental values at 1.3–1.4 eV [21,24,25]. Agreement with experiments shows that although DFT is known to perform poorly in predicting energy gaps, it can provide a good estimation of the optical gap of TMD monolayers [40], and this remains the case for heterostructures.

## IV. CONCLUSIONS

We performed first-principles calculations for Gr/TMD and TMD/TMD heterobilayers with near-zero strain by construction, and we examined their electronic properties as a function of the twist angle. We introduced a neat band structure representation for vdWH which allows for a straightforward comparison with their constituent monolayers. Interlayer interactions in Gr/TMD have negligible effects so that the Dirac cone of Gr remains unaffected and the TMD electronic band gap modifications are due to the very small strain (less than 1%) remaining in simulation cells. As a result of the interaction with Gr, the Fermi level moves closer to the CBM of the TMD (*n*-doping), and energy gaps are slightly reduced. This redshift of about 10 meV is universal, and it is also found in TMD/TMD heterobilayers. Interactions between TMD monolayers result in hybridization of electronic states and energy eigenvalues split around the $\Gamma$ point. The magnitude of energy splitting depends on the interlayer distance and determines the VBM. We find that interlayer transitions are more probable in $WSe_2/MoSe_2$ than $WS_2/MoS_2$. In addition to the general trends and universal results presented here, we believe that when excitonic effects are included, our theoretical approach provides the possibility to make a detailed and quantitative comparison with experimental techniques such as photoluminescence (PL) and angle-resolved photoemission spectroscopy on a case-by-case basis, with the goal to fully understand the physics of vdWH.

[1] K. S. Novoselov, A. K. Geim, S. V. Morozov, D. Jiang, Y. Zhang, S. V. Dubonos, I. V. Grigorieva, and A. A. Firsov, Electric field effect in atomically thin carbon films, Science **306**, 666 (2004).

[2] A. H. Castro Neto, F. Guinea, N. M. R. Peres, K. S. Novoselov, and A. K. Geim, The electronic properties of graphene, Rev. Mod. Phys. **81**, 109 (2009).

[3] K. S. Novoselov, D. Jiang, F. Schedin, T. J. Booth, V. V. Khotkevich, S. V. Morozov, and A. K. Geim, Two-dimensional atomic crystals, Proc. Natl. Acad. Sci. USA **102**, 10451 (2005).

[4] A. Kolobov and J. Tominaga, *Two-Dimensional Transition-Metal Dichalcogenides* (Springer, New York, 2016).

[5] K. F. Mak, C. Lee, J. Hone, J. Shan, and T. F. Heinz, Atomically Thin $MoS_2$: A New Direct-Gap Semiconductor, Phys. Rev. Lett. **105**, 136805 (2010).

[6] A. Splendiani, L. Sun, Y. Zhang, T. Li, J. Kim, C.-Y. Chim, G. Galli, and F. Wang, Emerging photoluminescence in monolayer $MoS_2$, Nano Lett. **10**, 1271 (2010).

[7] F. Xia, H. Wang, D. Xiao, M. Dubey, and A. Ramasubramaniam, Two-dimensional material nanophotonics, Nat. Photon **8**, 899 (2014).

[8] S. Manzeli, D. Ovchinnikov, D. Pasquier, O. V. Yazyev, and A. Kis, 2D transition metal dichalcogenides, Nat. Rev. Mater. **2**, 17033 (2017).

[9] X. Liu and M. C. Hersam, 2D materials for quantum information science, Nat. Rev. Mater. **4**, 669 (2019).

[10] B. Hinnemann, P. G. Moses, J. Bonde, K. P. Jørgensen, J. H. Nielsen, S. Horch, I. Chorkendorff, and J. K. Nørskov, Biomimetic hydrogen evolution: $MoS_2$ nanoparticles as catalyst for hydrogen evolution, J. Am. Chem. Soc. **127**, 5308 (2005).

[11] Z. W. Seh, J. Kibsgaard, C. F. Dickens, I. Chorkendorff, J. K. Nørskov, and T. F. Jaramillo, Combining theory and experiment in electrocatalysis: Insights into materials design, Science **355**, eaad4998 (2017).

[12] N. Mounet, M. Gibertini, P. Schwaller, D. Campi, A. Merkys, A. Marrazzo, T. Sohier, I. E. Castelli, A. Cepellotti, G. Pizzi, and N. Marzari, Two-dimensional materials from high-throughput computational exfoliation of experimentally known compounds, Nat. Nanotechnol. **13**, 246 (2018).

[13] A. K. Geim and I. V. Grigorieva, Van der Waals heterostructures, Nature (London) **499**, 419 (2013).

[14] K. S. Novoselov, A. Mishchenko, A. Carvalho, and A. H. Castro Neto, 2D materials and van der Waals heterostructures, Science **353**, aac9439 (2016).

[15] Y. Cao, V. Fatemi, S. Fang, K. Watanabe, T. Taniguchi, E. Kaxiras, and P. Jarillo-Herrero, Unconventional superconductivity in magic-angle graphene superlattices, Nature (London) **556**, 43 (2018).

[16] J. M. Park, Y. Cao, K. Watanabe, T. Taniguchi, and P. Jarillo-Herrero, Tunable strongly coupled superconductivity in magic-angle twisted trilayer graphene, Nature (London) **590**, 249 (2021).

[17] C. R. Dean, A. F. Young, I. Meric, C. Lee, L. Wang, S. Sorgenfrei, K. Watanabe, T. Taniguchi, P. Kim, K. L. Shepard, and J. Hone, Boron nitride substrates for high-quality graphene electronics, Nat. Nanotechnol. **5**, 722 (2010).

[18] Y. Liu, H. Wu, H.-C. Cheng, S. Yang, E. Zhu, Q. He, M. Ding, D. Li, J. Guo, N. O. Weiss, Y. Huang, and X. Duan, Toward barrier free contact to molybdenum disulfide using graphene electrodes, Nano Lett. **15**, 3030 (2015).

[19] X. Cui, G.-H. Lee, Y. D. Kim, G. Arefe, P. Y. Huang, C.-H. Lee, D. A. Chenet, X. Zhang, L. Wang, F. Ye, F. Pizzocchero, B. S. Jessen, K. Watanabe, T. Taniguchi, D. A. Muller, T. Low, P. Kim, and J. Hone, Multi-terminal transport measurements of $MoS_2$ using a van der Waals heterostructure device platform, Nat. Nanotechnol. **10**, 534 (2015).

[20] Y. Gong, J. Lin, X. Wang, G. Shi, S. Lei, Z. Lin, X. Zou, G. Ye, R. Vajtai, B. I. Yakobson, H. Terrones, M. Terrones, B. Tay, J. Lou, S. T. Pantelides, Z. Liu, W. Zhou, and P. M. Ajayan, Vertical and in-plane heterostructures from $WS_2/MoS_2$ monolayers, Nat. Mater. **13**, 1135 (2014).

[21] P. Rivera, J. R. Schaibley, A. M. Jones, J. S. Ross, S. Wu, G. Aivazian, P. Klement, K. Seyler, G. Clark, N. J. Ghimire, J. Yan, D. G. Mandrus, W. Yao, and X. Xu, Observation of long-lived interlayer excitons in monolayer $MoSe_2$-$WSe_2$ heterostructures, Nat. Commun. **6**, 6242 (2015).

[22] A. F. Rigosi, H. M. Hill, Y. Li, A. Chernikov, and T. F. Heinz, Probing interlayer interactions in transition metal dichalcogenide heterostructures by optical spectroscopy: $MoS_2/WS_2$ and $MoSe_2/WSe_2$, Nano Lett. **15**, 5033 (2015).

[23] M. Okada, A. Kutana, Y. Kureishi, Y. Kobayashi, Y. Saito, T. Saito, K. Watanabe, T. Taniguchi, S. Gupta, Y. Miyata, B. I. Yakobson, H. Shinohara, and R. Kitaura, Direct and indirect interlayer excitons in a van der Waals heterostructure of $hBN/WS_2/MoS_2/hBN$, ACS Nano **12**, 2498 (2018).

[24] K. L. Seyler, P. Rivera, H. Yu, N. P. Wilson, E. L. Ray, D. G. Mandrus, J. Yan, W. Yao, and X. Xu, Signatures of moiré-trapped valley excitons in $MoSe_2/WSe_2$ heterobilayers, Nature (London) **567**, 66 (2019).

[25] K. Tran, G. Moody, F. Wu, X. Lu, J. Choi, K. Kim, A. Rai, D. A. Sanchez, J. Quan, A. Singh, J. Embley, A. Zepeda, M. Campbell, T. Autry, T. Taniguchi, K. Watanabe, N. Lu, S. K. Banerjee, K. L. Silverman, S. Kim, E. Tutuc, L. Yang, A. H. MacDonald, and X. Li, Evidence for moiré excitons in van der Waals heterostructures, Nature (London) **567**, 71 (2019).

[26] E. Lorchat, L. E. P. López, C. Robert, D. Lagarde, G. Froehlicher, T. Taniguchi, K. Watanabe, X. Marie, and S. Berciaud, Filtering the photoluminescence spectra of atomically thin semiconductors with graphene, Nat. Nanotechnol. **15**, 283 (2020).

[27] R. M. Yunus, H. Endo, M. Tsuji, and H. Ago, Vertical heterostructures of $MoS_2$ and graphene nanoribbons grown by two-step chemical vapor deposition for high-gain photodetectors, Phys. Chem. Chem. Phys. **17**, 25210 (2015).

[28] T. Han, H. Liu, S. Wang, S. Chen, and K. Yang, Research on the preparation and spectral characteristics of Graphene/TMDs heterostructures, Nanoscale Res. Lett. **15**, 219 (2020).

[29] P. K. Nayak, Y. Horbatenko, S. Ahn, G. Kim, J.-U. Lee, K. Y. Ma, A.-R. Jang, H. Lim, D. Kim, S. Ryu, H. Cheong, N. Park, and H. S. Shin, Probing evolution of twist-angle-dependent interlayer excitons in $MoSe_2/WSe_2$ van der waals heterostructures, ACS Nano **11**, 4041 (2017).

[30] A. E. Maniadaki and G. Kopidakis, Hydrogen on hybrid $MoS_2$/graphene nanostructures, Phys. Status Solidi RRL **10**, 453 (2016).

[31] H.-P. Komsa and A. V. Krasheninnikov, Electronic structures and optical properties of realistic transition metal dichalcogenide heterostructures from first principles, Phys. Rev. B **88**, 085318 (2013).

[32] S. Latini, K. T. Winther, T. Olsen, and K. S. Thygesen, Interlayer excitons and band alignment in $MoS_2/hBN/WSe_2$ van der Waals heterostructures, Nano Lett. **17**, 938 (2017).

[33] V. Popescu and A. Zunger, Effective Band Structure of Random Alloys, Phys. Rev. Lett. **104**, 236403 (2010).

[34] V. Popescu and A. Zunger, Extracting $E$ versus $\vec{k}$ effective band structure from supercell calculations on alloys and impurities, Phys. Rev. B **85**, 085201 (2012).

[35] J. Voit, L. Perfetti, F. Zwick, H. Berger, G. Margaritondo, G. Grüner, H. Höchst, and M. Grioni, Electronic structure of solids with competing periodic potentials, Science **290**, 501 (2000).

[36] W. Ku, T. Berlijn, and C.-C. Lee, Unfolding First-Principles Band Structures, Phys. Rev. Lett. **104**, 216401 (2010).

[37] S. G. Mayo, F. Yndurain, and J. M. Soler, Band unfolding made simple, J. Phys.: Condens. Matter **32**, 205902 (2020).

[38] A. Deltsidis, L. Simonelli, G. Vailakis, I. C. Berdiell, G. Kopidakis, A. Krztoń-Maziopa, E. S. Bozin, and A. Lappas, $Li_x(C_5H_5N)_yFe_{2-z}Se_2$: A defect-resilient expanded-lattice high-temperature superconductor, Inorg. Chem. **61**, 12797 (2022).

[39] J. T. Paul, A. K. Singh, Z. Dong, H. Zhuang, B. C. Revard, B. Rijal, M. Ashton, A. Linscheid, M. Blonsky, D. Gluhovic, J. Guo, and R. G. Hennig, Computational methods for 2D materials: discovery, property characterization, and application design, J. Condens. Matter Phys. **29**, 473001 (2017).

[40] A. E. Maniadaki, G. Kopidakis, and I. N. Remediakis, Strain engineering of electronic properties of transition metal dichalcogenide monolayers, Solid State Commun. **227**, 33 (2016).

[41] P. E. Blöchl, Projector augmented-wave method, Phys. Rev. B **50**, 17953 (1994).

[42] G. Kresse and D. Joubert, From ultrasoft pseudopotentials to the projector augmented-wave method, Phys. Rev. B **59**, 1758 (1999).

[43] J. P. Perdew, M. Ernzerhof, and K. Burke, Rationale for mixing exact exchange with density functional approximations, J. Chem. Phys. **105**, 9982 (1996).

[44] G. Kresse and J. Furthmüller, Efficiency of ab-initio total energy calculations for metals and semiconductors using a plane-wave basis set, Comput. Mater. Sci. **6**, 15 (1996).

[45] G. Kresse and J. Furthmüller, Efficient iterative schemes for ab initio total-energy calculations using a plane-wave basis set, Phys. Rev. B **54**, 11169 (1996).

[46] S. N. Steinmann and C. Corminboeuf, A generalized-gradient approximation exchange hole model for dispersion coefficients, J. Chem. Phys. **134**, 044117 (2011).

[47] S. N. Steinmann and C. Corminboeuf, Comprehensive benchmarking of a density-dependent dispersion correction, J. Chem. Theory Comput. **7**, 3567 (2011).

[48] V. M. Pereira, A. H. Castro Neto, and N. M. R. Peres, Tight-binding approach to uniaxial strain in graphene, Phys. Rev. B **80**, 045401 (2009).

[49] H. J. Conley, B. Wang, J. I. Ziegler, R. F. Haglund, S. T. Pantelides, and K. I. Bolotin, Bandgap engineering of strained monolayer and bilayer $MoS_2$, Nano Lett. **13**, 3626 (2013).

[50] See Supplemental Material at http://link.aps.org/supplemental/10.1103/PhysRevMaterials.7.024004 for additional figures and tables.

[51] G. A. Tritsaris, Y. Xie, A. M. Rush, S. Carr, M. Mattheakis, and E. Kaxiras, LAN: A materials notation for two-dimensional layered assemblies, J. Chem. Inf. Model. **60**, 3457 (2020).

[52] M. R. Rosenberger, H.-J. Chuang, M. Phillips, V. P. Oleshko, K. M. McCreary, S. V. Sivaram, C. S. Hellberg, and B. T. Jonker, Twist angle-dependent atomic reconstruction and moiré patterns in transition metal dichalcogenide heterostructures, ACS Nano **14**, 4550 (2020).

[53] S. Carr, D. Massatt, S. B. Torrisi, P. Cazeaux, M. Luskin, and E. Kaxiras, Relaxation and domain formation in incommensurate two-dimensional heterostructures, Phys. Rev. B **98**, 224102 (2018).

[54] J. Quan, L. Linhart, M.-L. Lin, D. Lee, J. Zhu, C.-Y. Wang, W.-T. Hsu, J. Choi, J. Embley, C. Young, T. Taniguchi, K. Watanabe, C.-K. Shih, K. Lai, A. H. MacDonald, P.-H. Tan, F. Libisch, and X. Li, Phonon renormalization in reconstructed $MoS_2$ moiré superlattices, Nat. Mater. **20**, 1100 (2021).